

See discussions, stats, and author profiles for this publication at: <https://www.researchgate.net/publication/235191774>

A 3D-Object Reconstruction System Integrating Range-Image Processing and Rapid Prototyping

Article · December 1990

DOI: 10.1007/978-94-011-2560-4_38

CITATIONS

4

READS

43

4 authors, including:



Carlos Cerrada

National Distance Education University

107 PUBLICATIONS 520 CITATIONS

[SEE PROFILE](#)



Katsushi Ikeuchi

Microsoft

805 PUBLICATIONS 16,357 CITATIONS

[SEE PROFILE](#)

Some of the authors of this publication are also working on these related projects:



COLISEE (Linguistic, Intercultural and Entrepreneurial Competences Serving Businesses in Europe) [View project](#)



DESIGN, DEVELOPMENT AND APPLICATION OF RECONSTRUCTION TECHNIQUES AND VISUALIZATION OF COMPLEX 3D SCENES USING RANGE SENSORS [View project](#)

AD-A233 577



12

A 3D-Object Reconstruction System Integrating Range-Image Processing and Rapid Prototyping

Carlos Cerrada, Katsushi Ikeuchi, Lee Weiss, Raj Reddy

CMU-RI-TR-90-32



The Robotics Institute
Carnegie Mellon University
Pittsburgh, PA 15213

December 1990

© Carnegie Mellon University

This research was conducted in the Task Oriented Vision Laboratory, VAS' and The Shape Deposition Laboratory, The Robotics Institute, Carnegie Mellon University. Carlos Cerrada is on leave of absence from National University of Education at Distance (UNED), Madrid Spain, and under support of a MEC/Fulbright grant.



91 3 14 048

REPORT DOCUMENTATION PAGE			Form Approved OMB No. 0704-0188	
<small>Public reporting burden for this collection of information is estimated to average 1 hour per response, including the time for reviewing instructions, searching existing data sources, gathering and maintaining the data needed, and completing and reviewing the collection of information. Send comments regarding this burden estimate or any other aspect of this collection of information, including suggestions for reducing this burden, to Washington Headquarters Services, Directorate for Information Operations and Reports, 1215 Jefferson Davis Highway, Suite 1204, Arlington, VA 22202-4302, and to the Office of Management and Budget, Paperwork Reduction Project (0704-0188), Washington, DC 20503.</small>				
1. AGENCY USE ONLY (Leave blank)	2. REPORT DATE December 1990	3. REPORT TYPE AND DATES COVERED Technical		
4. TITLE AND SUBTITLE A 3D-Object Reconstruction System Integrating Range-Image Processing and Rapid Prototyping		5. FUNDING NUMBERS		
6. AUTHOR(S) Carlos Cerrada, Katsushi Ikeuchi, Lee Weiss, Raj Reddy				
7. PERFORMING ORGANIZATION NAME(S) AND ADDRESS(ES) The Robotics Institute Carnegie Mellon University Pittsburgh, PA 15213		8. PERFORMING ORGANIZATION REPORT NUMBER CMU-RI-TR-90-32		
9. SPONSORING / MONITORING AGENCY NAME(S) AND ADDRESS(ES)		10. SPONSORING / MONITORING AGENCY REPORT NUMBER		
11. SUPPLEMENTARY NOTES				
12a. DISTRIBUTION / AVAILABILITY STATEMENT Approved for public release; Distribution unlimited		12b. DISTRIBUTION CODE		
13. ABSTRACT (Maximum 200 words) This paper describes a system which integrates computer vision and rapid manufacturing technologies to scan physical objects and to replicate the reconstructed shapes as steel faced dies using shaping deposition processes. A light-stripe range finder is used to scan the 3-D data of the object. Range data is then processed in order to generate a solid model representation. A simulation process is incorporated to display the reconstructed object so that data quality is checked and refined before proceeding to the fabrication process, as well as viewing object in alternative materials and colors. The computer model is then replicated as a plastic prototype is used as a pattern in a thermal spray process to build a metal-faced die replica of the original object. The system is demonstrated by scanning a human face which is then replicated as a stainless-steel sculpture.				
14. SUBJECT TERMS		15. NUMBER OF PAGES 34 pp		
		16. PRICE CODE		
17. SECURITY CLASSIFICATION OF REPORT Unlimited	18. SECURITY CLASSIFICATION OF SUMMARY Unlimited	19. SECURITY CLASSIFICATION OF ABSTRACT Unlimited	20. LIMITATION OF ABSTRACT	

Contents

1	Introduction	1
2	Object Scanning	2
3	Data Reconstruction Module	4
3.1	Filtering and Face Extraction	4
3.1.1	Face Area Selection	4
3.1.2	Noise Elimination	5
3.1.3	Coordinate Frame Conversion	7
3.2	Computer Model Generator	9
3.2.1	Face Area Tessellation	10
3.2.2	Contour Area Tessellation	10
3.2.3	Bottom Area Tessellation	12
3.3	Simulation Process based on Ray-Tracer	13
3.3.1	Reflectance Model	13
3.3.2	Organization of the Simulator	15
3.3.3	Simulation Results	15
4	Rapid Fabrication Module	17
4.1	Stereolithography Process	19
4.2	Thermal Spraying Process	19
5	Summary	24
A	Reflectance Model Fundamentals	28
A.1	Beckmann-Spizzichino Model	28
A.2	Lambertian Model	34



Accession For	
NTIS CRA&I	<input checked="" type="checkbox"/>
DTIC TAB	<input type="checkbox"/>
Unannounced	<input type="checkbox"/>
Justification	
By	
Distribution/	
Availability Codes	
Dist	Availability Codes
A-1	Special

List of Figures

1	Block diagram of the system	3
2	OGIS range finder setup	4
3	Original images provided by the range finder	5
4	Aspect of the 3D input range data	6
5	Face area selection steps	7
6	Relationship between the range finder coordinate system and the coordinate system required in the stereolithography module	8
7	Aspect of the 3D converted range data	9
8	Graphical description of the tessellation algorithm	11
9	Polar plots of the three reflection components as functions of the viewing angle for a fixed source direction.	14
10	Geometry of the ray-tracer mechanism	16
11	Sensor and source light geometric distribution to obtain 16 sequential images . . .	17
12	Images obtained considering different simulation conditions	18
13	Stereolithography apparatus scheme	20
14	Aspect of the plastic sculpture	21
15	Electric arc spraying	22
16	Graphical description of thermal spraying process	23
17	Final aspect of the sculpture in steel	24
18	Coordinate system to derive the Beckmann-Spizzichino model	29
19	Image formation	33

ABSTRACT

This paper describes a system which integrates computer vision and rapid manufacturing technologies to scan physical objects and to replicate the reconstructed shapes as steel faced dies using shaping deposition processes. A light-stripe range finder is used to scan the 3-D data of the object. Range data is then processed in order to generate a solid model representation. A simulation process is incorporated to display the reconstructed object so that data quality is checked and refined before proceeding to the fabrication process, as well as viewing object in alternative materials and colors. The computer model is then replicated as a plastic prototype with stereolithography. Finally, this prototype is used as a pattern in a thermal spray process to build a metal-faced die replica of the original object. The system is demonstrated by scanning a human face which is then replicated as a stainless-steel sculpture.

1 Introduction

Manufacturing technology has experienced a significant improvement in productivity in the recent years due in part to the development of Computer Integrated Manufacturing (CIM) and its enabling technologies. Two such technologies are computer vision systems and solid-freeform-fabrication (SFF) processes. While these technologies have unique roles in rapid object scanning/reconstruction and rapid part fabrication applications, respectively, their integration can produce novel rapid object replication systems. This paper describes a prototype object replication system which produces steel-faced dies from scanned object models. While the system has been demonstrated by fabricating a stainless steel sculpture of a scanned human face, it also has industrial significance. In principal therefore, we can go from clay sculpture of a new car design to stamping die to make prototype metal hoods.

In conventional CIM systems the parts to be produced are first defined using Computer Aided Design (CAD) tools. Computer vision may then be applied in subsequent manufacturing stages, such as part recognition and inspection using model-based vision techniques. Computer vision, however, can also help manufacturing in other novel ways. Consider an alternative situation where the model of a part to be evaluated or to be fabricated first comes from a physical object instead of being a computer generated model. For example automobile designs may originate as a clay sculpture of a new car body. The shape of the object must then be encoded into a CAD data base. In such cases the object can be scanned by means of a coordinate measuring machine (CMM) or by computer vision. Computer vision has the potential to be faster and to produce a higher density of sample points than CMM. After the data is gathered, it must then be transformed into a valid computer representation of the object for use in subsequent CIM operations. For example, Finnigan [6] has recently developed a system which takes computer-aided tomography (CAT) scans of industrial parts, and converts them into finite element models. The technique allows newly manufactured designs to be checked against their specified dimensions and for preforming subsequent finite element analysis. In another example, Choi [2] describes an algorithm to transform sampled points from scanned 3-D data to surface and solid representations using a non-manifold geometric modeling system. Plastic prototypes of valid solid models are then fabricated with stereolithography as described below.

Another important CIM development is in the area of rapid prototyping and rapid tool manufacturing. In these systems CAD part representations drive novel SFF processes to quickly produce both prototypes and tools (i.e., tools to manufacture the parts in quantity) without machining operations [18]. Combining the object scanning/shape reconstruction capabilities of computer vision with the rapid fabrication capabilities of SFF enable novel rapid object replication processes to be implemented. For example, a commercialized object replication system manufactured by Cyberware Laboratory (Monterey, California) uses an optical range-finding system to scan the object and then replicates it with a desk-top CNC machine. CNC operations, however, are more difficult to plan and are therefore more costly than SFF. The SFF technologies can build parts of arbitrary geometric complexity, but are currently less precise than those produced by CNC machining.

The system presented in this paper integrates computer vision and rapid manufacturing technologies to scan physical objects and to replicate the reconstructed shapes as metal faced dies

using SFF processes. The system is composed of several modules including: scanner, data reconstruction, stereolithography, and thermal spraying (Figure 1). The system incorporates several novel technologies including a simulation stage, based upon ray tracing techniques, which enables a designer to view synthetic images of the metal object from several perspectives and assess its appearance before proceeding to the building stages. Whenever irregularities are detected the reconstruction stages are reiterated until a satisfactory result is achieved. The system also includes a novel thermal spray process which enables the rapid fabrication of steel-faced dies. Previous spray technology has been limited to softer metals such as zinc alloys.

Next section of the paper contains an explanation of the object scanning procedure. Section 3 is devoted to explain the Data Reconstruction Module of the system. Intermediate appearances of the processed data and several simulation results are also included in this section. The Rapid Fabrication Module is explained in section 4. Concluding remarks are gathered in the summary section.

2 Object Scanning

Figure 2 shows the setup of the object scanning system which consists of a slide projector with a liquid crystal shutter [16], a CCD TV camera, and a point light source. The range finder provides three images, $X(i,j)$, $Y(i,j)$, $Z(i,j)$, which contain the world coordinates of the pixel, (i,j) . Another additional intensity image $I(i,j)$ of the scene is also provided at the same time. Range resolution rounds 1.5mm for this specific setup. Accuracy depends on calibration but it is around 0.5mm in the actual implementation. Provided range images are 240 by 256 pixels wide and less resolution is obtained in practical just by using image demagnification procedures. Figure 3 shows the four input images as they are given by the range finder. Notice that Y coordinate remains almost constant over image column, and Z coordinate does so at every row. This is because the image plane of the sensor is parallel to the world YZ plane.

The range finder generates depth information as follows. A set of coded light striped patterns are sequentially projected onto the scene (i.e., object plus background). Whenever a striped pattern is projected, an associate intensity image is registered. Afterwards, the set of intensity images are decoded and, by using simple triangularization, the distance from the camera to the point represented at every pixel (i,j) is easily computed and then transformed to the world coordinate system.

Several measurement errors are generated in the process of scanning a human face in part because it is difficult to remain perfectly motionless during scanning. Other sources of inherent sensor noise and measurement error exist. An example of the measured data is shown in Figure 4 which contains a wire-frame representation of the 3D data registered in the input range data. The noisy images are processed in the Data Reconstruction Module which is described in the following section.

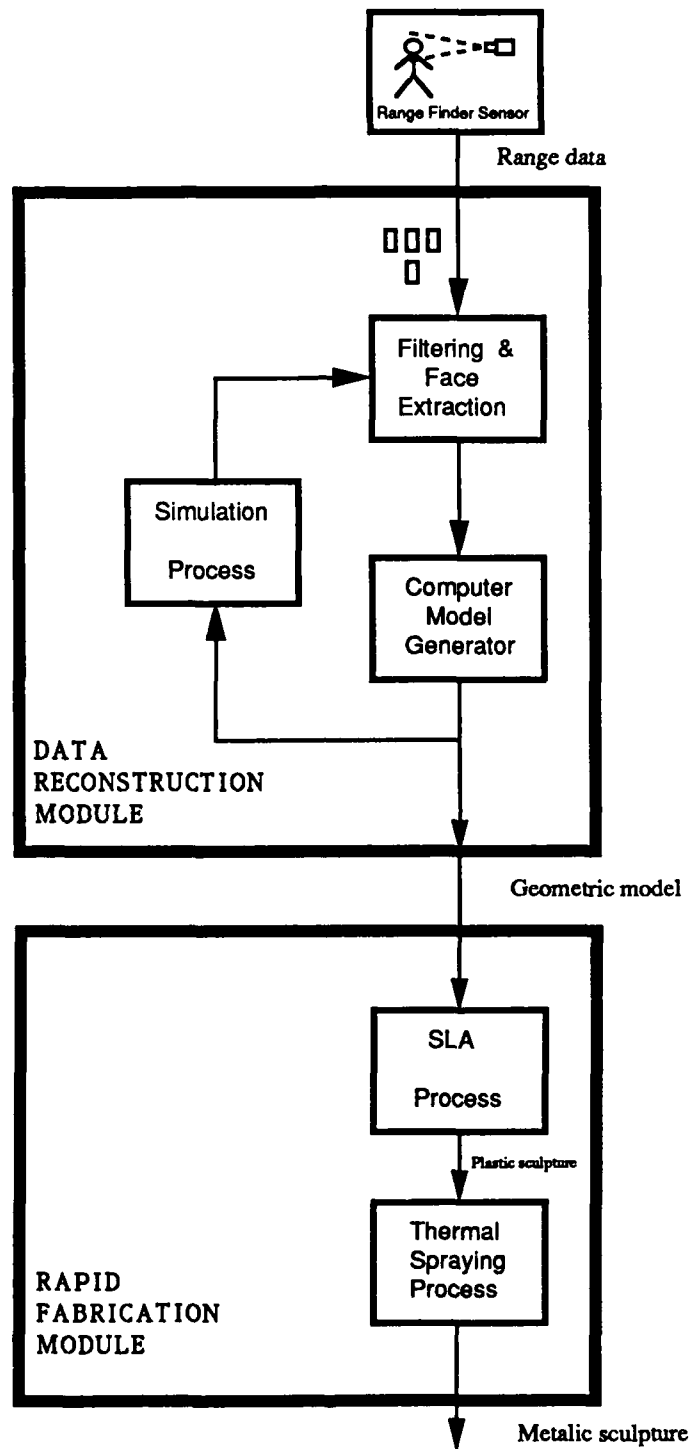


Figure 1: Block diagram of the system

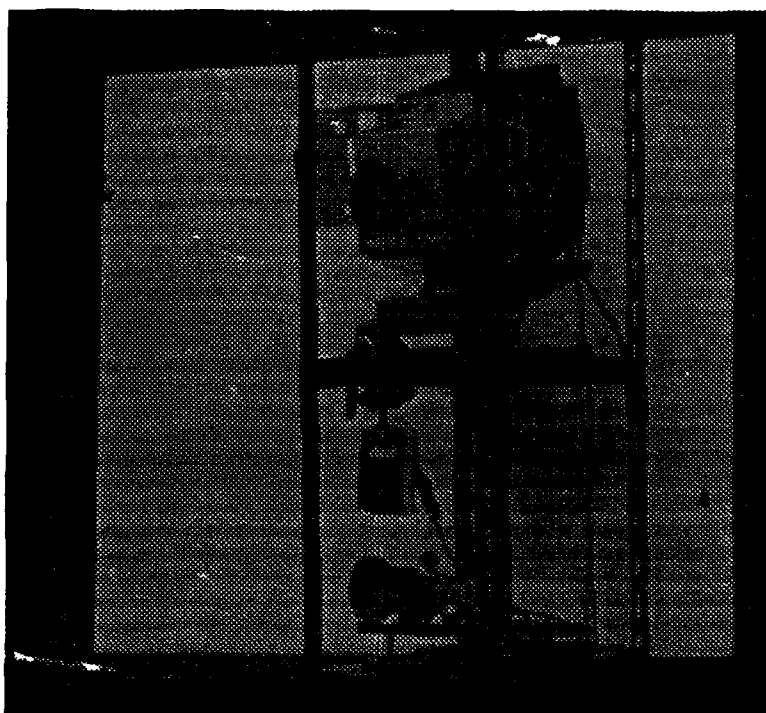


Figure 2: OGIS range finder setup

3 Data Reconstruction Module

The Data Reconstruction Module is organized into three blocks that close a loop as indicated in Figure 1. In the first block a filtering and feature extraction stage is carried out on the input range data images. The second block is the computer model generator which tessellates the converted range images and creates the solid representation. The third block is the simulation process which provides visual feedback to detect the remaining errors. These three blocks are explained in more detail next.

3.1 Filtering and Face Extraction

Image processing algorithms are applied here to clean the input range images and to extract from them the information required to generate the geometric model of the face. The following subsections describe the sequence of filters and extraction operations.

3.1.1 Face Area Selection

The present application of this work is only interested in facial region and is not concerned with the rest of the body that may appear in the scene. Therefore, background and other body features

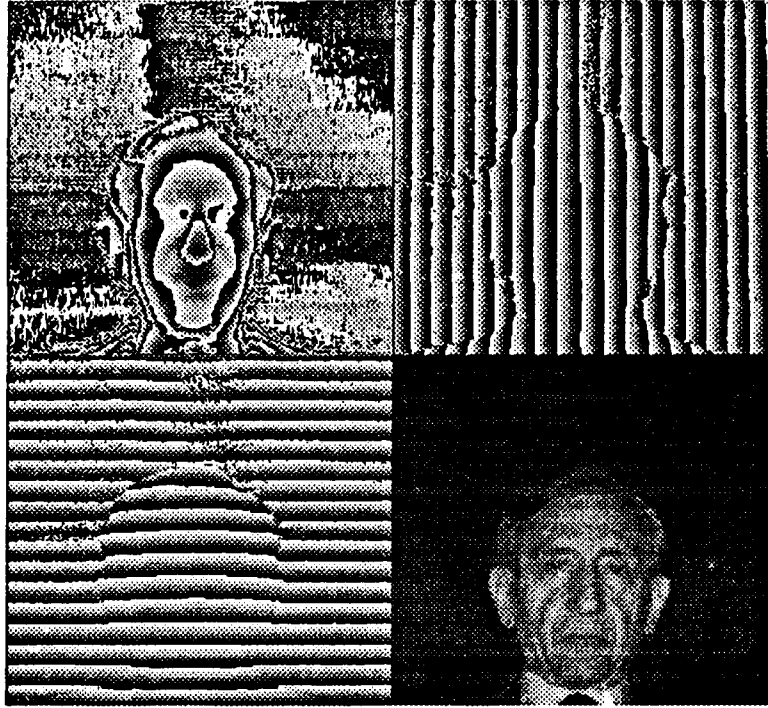


Figure 3: Original images provided by the range finder: $X(i, j)$ (up-left), $Y(i, j)$ (up-right), $Z(i, j)$ (bottom-left) and $I(i, j)$ (bottom-right)

such as neck or shoulders have to be removed to isolate the face. In order to do this, several image processing algorithms have been used.

A Sobel operator is the first image processing operator applied to the depth image, $X(i, j)$, to find the edges which, in this case, represent depth discontinuities. The resulting sobel image is shown in Figure 5. It is clear that no uniform region with large Sobel values are apparent in the background area. The obtained range image contains some noise, however it is not concentrated in any specific region in the Sobel image. On the contrary, several uniform and narrow regions with bigger sobel values can be observed in the face and body contours. A threshold is then chosen and a segmentation is performed in such a way that a set of disconnected regions appear, as can be seen in Figure 5. The biggest region is selected as the face area and all the others are discarded. After smoothing and interpolation, a new image $X'(i, j)$ is created.

Using this new $X'(i, j)$ image as a mask, the associated $Y'(i, j)$ and $Z'(i, j)$ can be easily extracted from the input ones, thus obtaining a set of range images containing only the face area.

3.1.2 Noise Elimination

Spurious noise values are still detected in the X' coordinate, mainly in the boundaries of the selected face area, due in part to the range data acquisition process. By using a grassfire operator, a shrink-expand step is carried out. Several layers of the face area contour are removed in this

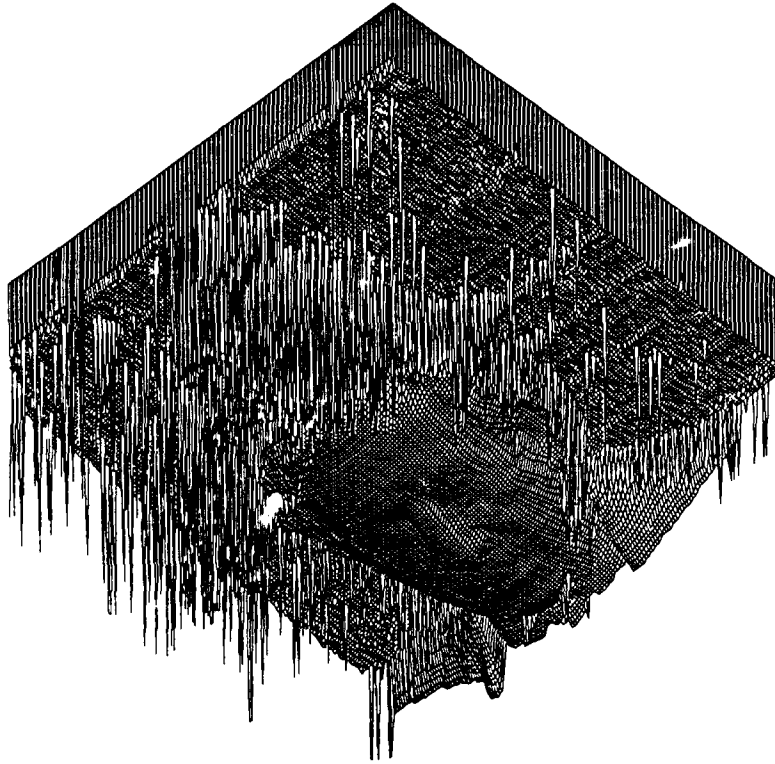


Figure 4: Aspect of the 3D input range data

step, eliminating the zone where erroneous values were observed. Small blob regions, previously connected to the main face region by narrow paths, are also removed in this step.

A different kind of noise problem was detected in the $Y'(i, j)$ and $Z'(i, j)$ images. As it was said in the previous section, image plane of the sensor is parallel to the world YZ plane, which implies that a linear relationship between the world coordinate system and the image coordinate system, as in:

$$\begin{aligned} Y'(i, j) &= \alpha i + Y'_{ini} \\ Z'(i, j) &= \beta j + Z'_{ini} \end{aligned} \quad (1)$$

should exist.

In practical, several errors were detected in the registered data at arbitrary pixel values (i_k, j_l) . Non-linear increments in the Y' or Z' coordinates were found in neighbor pixels, as for example in the following case:

$$\begin{aligned} Y'(i_1, j_1) - Y'(i_1 - 1, j_1) &> 0 \\ Y'(i_1 + 1, j_1) - Y'(i_1, j_1) &< 0, \end{aligned} \quad (2)$$

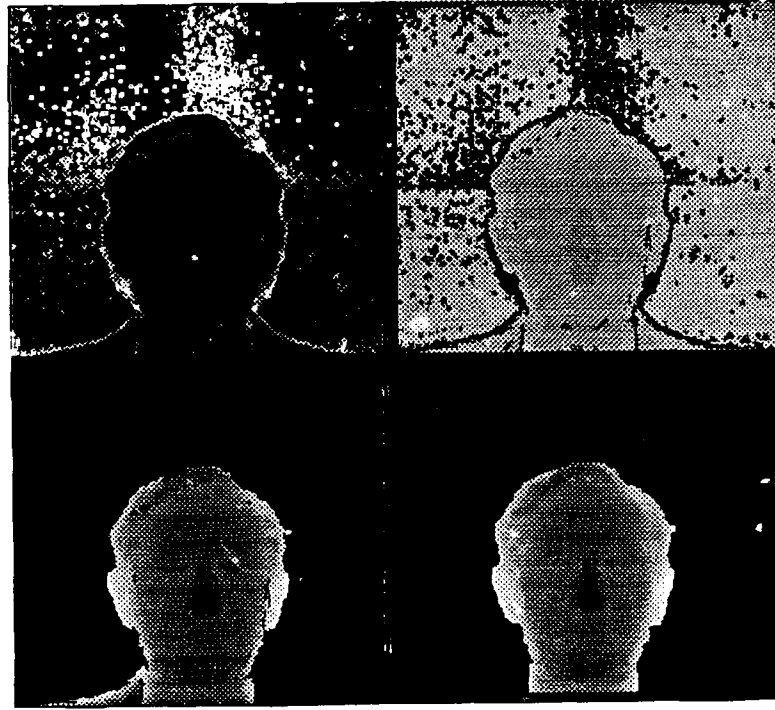


Figure 5: Face area selection steps: Sobel image (u-l), Segmented image (u-r), Selected biggest region (b-l), Smooth and interpolated image (b-r)

or in:

$$\begin{aligned} Z'(i_2, j_2) - Z'(i_2, j_2 - 1) &> 0 \\ Z'(i_2, j_2 + 1) - Z'(i_2, j_2) &< 0. \end{aligned} \quad (3)$$

Linearity was enforced by computing the parameters α , β , Y'_{ini} and Z'_{ini} from the existing $Y'(i, j)$ and $Z'(i, j)$ images, without lost of precision in range data. Then, both previous images were substituted by two other new ones which verify the linear equations (1).

3.1.3 Coordinate Frame Conversion

Figure 6 shows the relationship of the range finder with respect to the world coordinate system in this setup. Because of the special requirements of the stereolithography module, a coordinate frame transformation has to be performed before generating the solid representation. The new coordinate system specifications required by the stereolithography module are:

- The new Z_n coordinate must represent depth information.

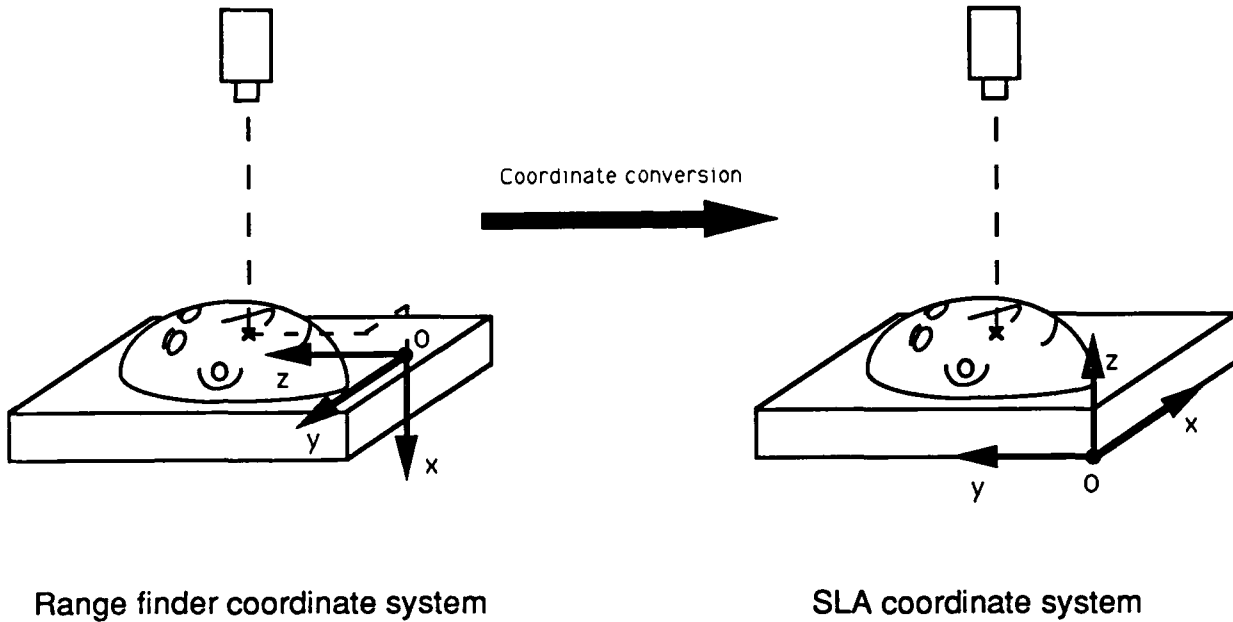


Figure 6: Relationship between the range finder coordinate system and the coordinate system required in the stereolithography module

- Every point represented in this coordinate system must have its three coordinate values positive.
- X_n and Y_n coordinates must be contained in a rectangular frame smaller than the size of the SLA vat where face will be reconstructed.

With these specifications a coordinate transformation has to be performed including axis rotation, translation and scaling. The equations of this transformation are:

$$\begin{aligned}
 X_n(i, j) &= off_x - [Y'(i, j) - Y'_{max}] * scale \\
 Y_n(i, j) &= off_y + [Z'(i, j) - Z'_{min}] * scale \\
 Z_n(i, j) &= off_z - [X'(i, j) - X'_{max}] * scale,
 \end{aligned} \tag{4}$$

where maximum and minimum values of each coordinate are previously computed, the *scale* factor is chosen to fit the face into the rectangular frame, and the *off_x* and *off_y* offset values, required to center the face in the frame, are obtained from the following expressions:

$$\begin{aligned}
 off_x &= (FRAME_x - [Y'_{max} - Y'_{min}] * scale) / 2 \\
 off_y &= (FRAME_y - [Z'_{max} - Z'_{min}] * scale) / 2.
 \end{aligned} \tag{5}$$

The off_z variable is a fixed value required by the SLA.

3.2 Computer Model Generator

The output of the previous stage is a set of three new range images $X_n(i, j)$, $Y_n(i, j)$ and $Z_n(i, j)$. They represent a set of points in the stereolithography module coordinate system that define, point by point, an irregular and open surface corresponding to the human face to be reproduced. Figure 7 shows the wire-frame representation of these 3D converted data.

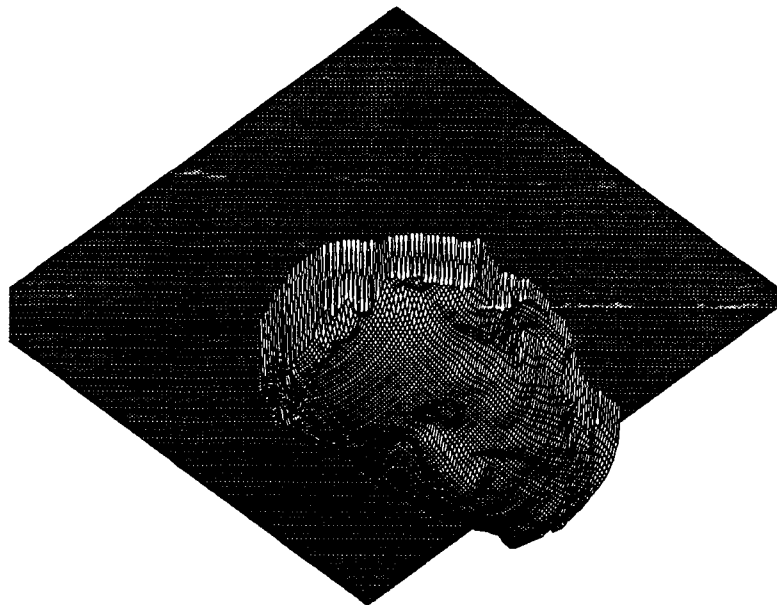


Figure 7: Aspect of the 3D converted range data

A valid solid geometric computer model must be generated from this data. A boundary representation is the required representation such that the object is described in terms of the set of its boundary surfaces which conform a closed surface. A tessellation technique has been used to generate the computer model from the actual range data, and it has been developed in three steps. The first one deals with the tessellation of the upward facing boundary surfaces which come directly from the face area points. The second step creates a completely synthetic wall-fashion surface obtained as a projection of the contour points of the face area. The last one deals with the task of closing the solid by creating a bottom boundary surface. The three steps for the tessellation procedure are outlined below.

Because of the stereolithography manufacturing requirements, the model of the solid must be translated to a planar faceted representation. This format consists of a series of sided facets and a corresponding facet normal.

Image resolution has a direct effect in the output file size and execution time of the computer model generator stage. The total number of facets generated in the face area tessellation step presents a second order decreasing ratio with the demagnification factor. The number of facets in the two other tessellation steps also decreases but only linearly with such a factor. On the other hand, human face features are in practical still neatly observable when using half the original image resolution, meanwhile they are greatly smoothed when a quarter of resolution is used.

3.2.1 Face Area Tessellation

In this step the face area points are combined to tessellate the surface which they belong to. Our approach deals with this task by scanning row by row the range images and taking every set of three neighbor points in order to create sets of small triangular facets. The triangularization algorithm has to fulfill several requirements:

- Every point must be considered to generate all the possible triangles. It means that no hole must appear in the surface description.
- Triangles must be complementary in the sense that no one must overlap each other, or no one must be generated more than once.
- Triangles in the boundary of the face area must connect with triangles that define the contour surfaces.

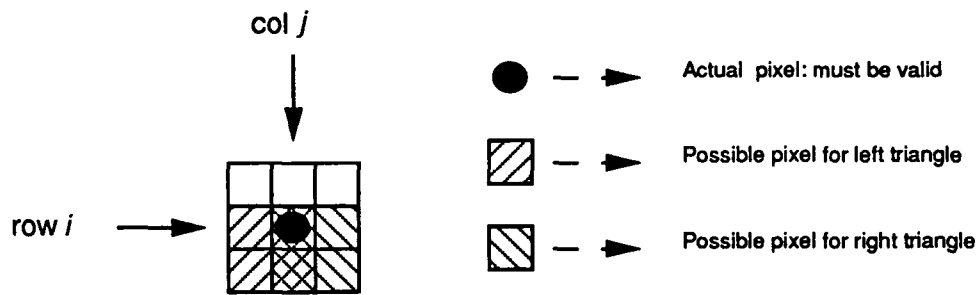
The algorithm developed here satisfies these restrictions and it is graphically shown in Figure 8. The solution consists of scanning the range images row by row. Every existing point may be part of at most two triangles, depending on the existence of the neighbor points. Given a valid pixel (i, j) the triangularization process is divided in two parts: the left triangle generation and the right triangle generation. The left triangle involves the pixels in the actual and previous columns and in the actual and next row, that is, $(i, j - 1)$, $(i + 1, j - 1)$, (i, j) and $(i + 1, j)$. The left triangle is generated only if both (i, j) and $(i, j + 1)$ pixels exist. Even in this case a third valid pixel is needed. Therefore the two other possible pixels in the window are scanned in a specific order. Pixel $(i + 1, j - 1)$ is searched for first and, if this one does not exist, pixel $(i, j - 1)$ is then considered. No left triangle is generated if none of them exist. The algorithm has the same structure when the right triangle is generated.

This simple solution is complete and fulfills the requirements. The most difficult restriction occurs in the contour connection, but it works perfectly if a 4-connectivity criterion is used to define connected regions.

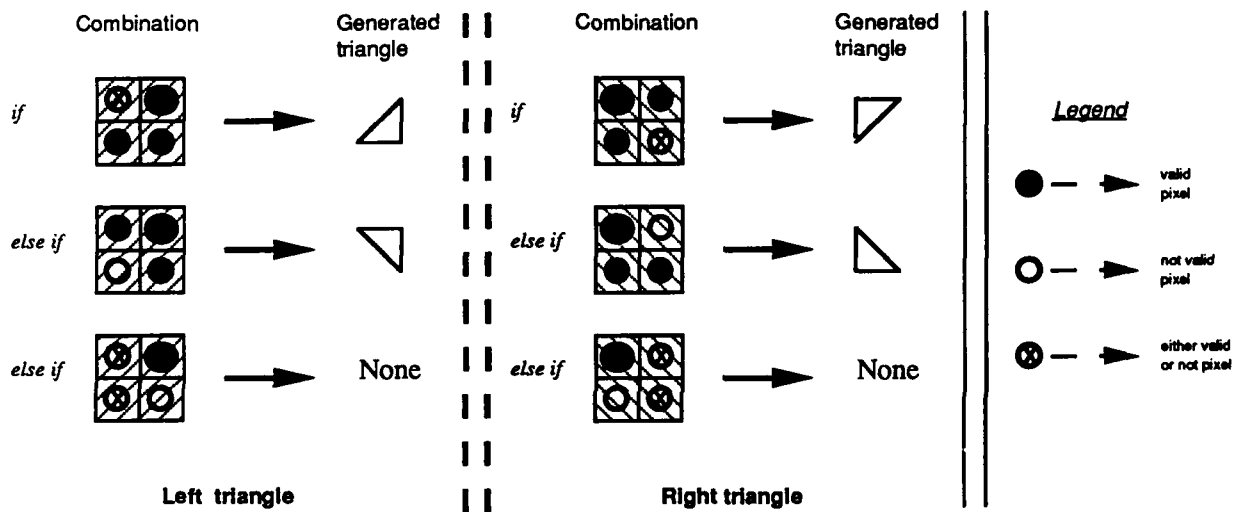
3.2.2 Contour Area Tessellation

A wall definition has to be defined to close the face in the lateral view. In order to do that, points belonging to the contour of the face need to be extracted. Then they are projected to obtain another set of points and finally neighbor points are tessellated to create triangles in the same way that the face area was created.

First pixel agrupation



Combination checking algorithm



Possibilities for the two-triangles set

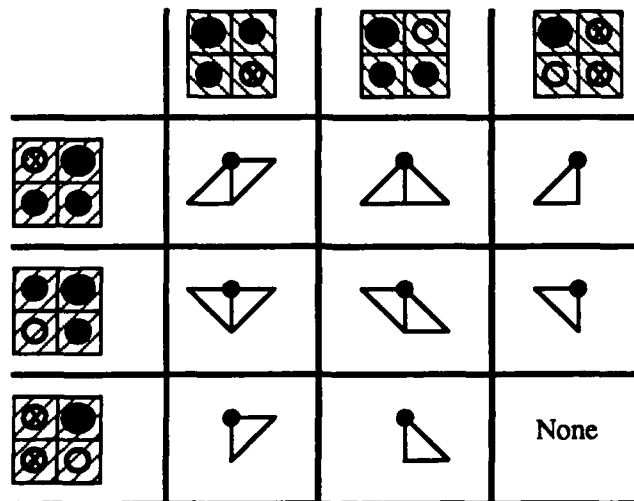


Figure 8: Graphical description of the tessellation algorithm

To obtain the contour points, a binary mask is first extracted from one of the three images, for example $X_n(i, j)$, and a polygon fitting algorithm is applied to this mask. The result is a list of m pixel values (i_l, j_l) that define the 4-connected contour of the mask. An array C of m points containing the 3D contour of the face are then generated from the list of pixels and the 3D images:

$$\begin{aligned} C_x(l) &= X_n(i_l, j_l) \\ C_y(l) &= Y_n(i_l, j_l) \\ C_z(l) &= Z_n(i_l, j_l). \end{aligned} \quad l = 1 \dots m \quad (6)$$

After the projection, the other set of m points are generated and stored in another array B :

$$\begin{aligned} B_x(l) &= C_x(l) \\ B_y(l) &= C_y(l) \\ B_z(l) &= Z_{nmin}, \end{aligned} \quad l = 1 \dots m \quad (7)$$

where Z_{nmin} is the minimum value of the Z_n coordinate in the set of m points of C . The last thing to do is tessellate $2m$ triangles with the two sets of points, combining in the following way:

$$\begin{aligned} \text{Triangle } l_1 : & \text{ Points } C(l), C(l+1) \text{ and } B(l) \quad l = 1 \dots m \\ \text{Triangle } l_2 : & \text{ Points } B(l), B(l+1) \text{ and } C(l+1) \quad l = 1 \dots m \end{aligned}$$

3.2.3 Bottom Area Tessellation

The closing surface in the bottom of the sculpture is generated also from the set of points B and a fixed point CC centered with respect to the face, and defined as:

$$\begin{aligned} CC_x &= FRAME_X/2 \\ CC_y &= FRAME_Y/2 \\ CC_z &= off_{z2}. \end{aligned} \quad (8)$$

This point CC is used as the vertex of a cone formed by the m points of B . The cone is tessellated with the m triangles as follows:

$$\text{Triangle } l : \text{ Points } B(l), B(l+1) \text{ and } CC \quad l = 1 \dots m$$

3.3 Simulation Process based on Ray-Tracer

There are several reasons to use a simulation process in this replication application. For example the user can observe what the sculpture will look like in alternative materials before committing to the actual building process. The user can see what is the effect of the closing areas defined in the previous stages to create a solid body. There is also a need to include a simulation process because it becomes necessary to close the loop in the refinement of the data generated to the fabrication process. Several imperfections due to noise may at this stage be detected, as well as forming errors. After the simulation, previous stages can be reiterated to obtain the desired results.

A simulation process based on ray-tracer technique has been developed to complete the Data Reconstruction Module. The reflectance model used in the simulator is described below. Specific implementation details of the simulation process applied to this project are then explained. Simulation results are finally shown.

3.3.1 Reflectance Model

There are two approaches to the study of reflection: physical and geometrical optics. While geometrical models may be construed as mere approximations to physical models, they possess simpler mathematical forms that often render them more usable than physical models. However, geometrical models are applicable only when the wavelength of incident light is small compared to the dimensions of the surface imperfections.

Nayar, Ikeuchi and Kanade [14] have proposed an unified reflectance model based on the Beckmann-Spizzichino physical optics model [1] and the Torrance-Sparrow geometric optics model [17]. It also includes the Lambertian model [13] which explains diffuse reflection mechanisms not very well explained in the two previous models. This unified model comprises three reflection components: the diffuse lobe, the specular lobe and the specular spike. They report identical results for both Beckmann-Spizzichino and Torrance-Sparrow models under certain restrictions, and conclude that, whenever the Torrance-Sparrow is simpler to formulate, the Beckmann-Spizzichino model is more general and explains better all the reflection mechanisms for different kind of surfaces, from smoother to rougher. Appendix A contains the basic Beckmann-Spizzichino and Lambertian models fundamentals on top of which the unified model is described. The simulator developed uses this unified model to represent the different reflection components, so a brief description of it is included next.

From the physical and geometrical optics reflection models, it can be seen [14] that surface radiance may be decomposed into three primary reflection components, namely, the diffuse lobe, specular lobe, and specular spike. Polar plots of these three components are illustrated in Figure 9. The sum of the three lobe components determines the surface radiance detected by the viewer for a fixed position of the source. The diffuse lobe is represented by the Lambertian model, and is constant with respect to the viewing direction. The specular lobe tends to be distributed around the specular direction, and has off-specular peaks for relatively large values of surface roughness. The specular spike is concentrated in a small region around the specular direction. The strengths of the specular lobe and specular spike components are related to one another. For a smooth surface, the specular spike component is many orders of magnitude greater than the specular lobe

component. As the surface roughness increases, the spike component shrinks rapidly, and the specular lobe begins to dominate.

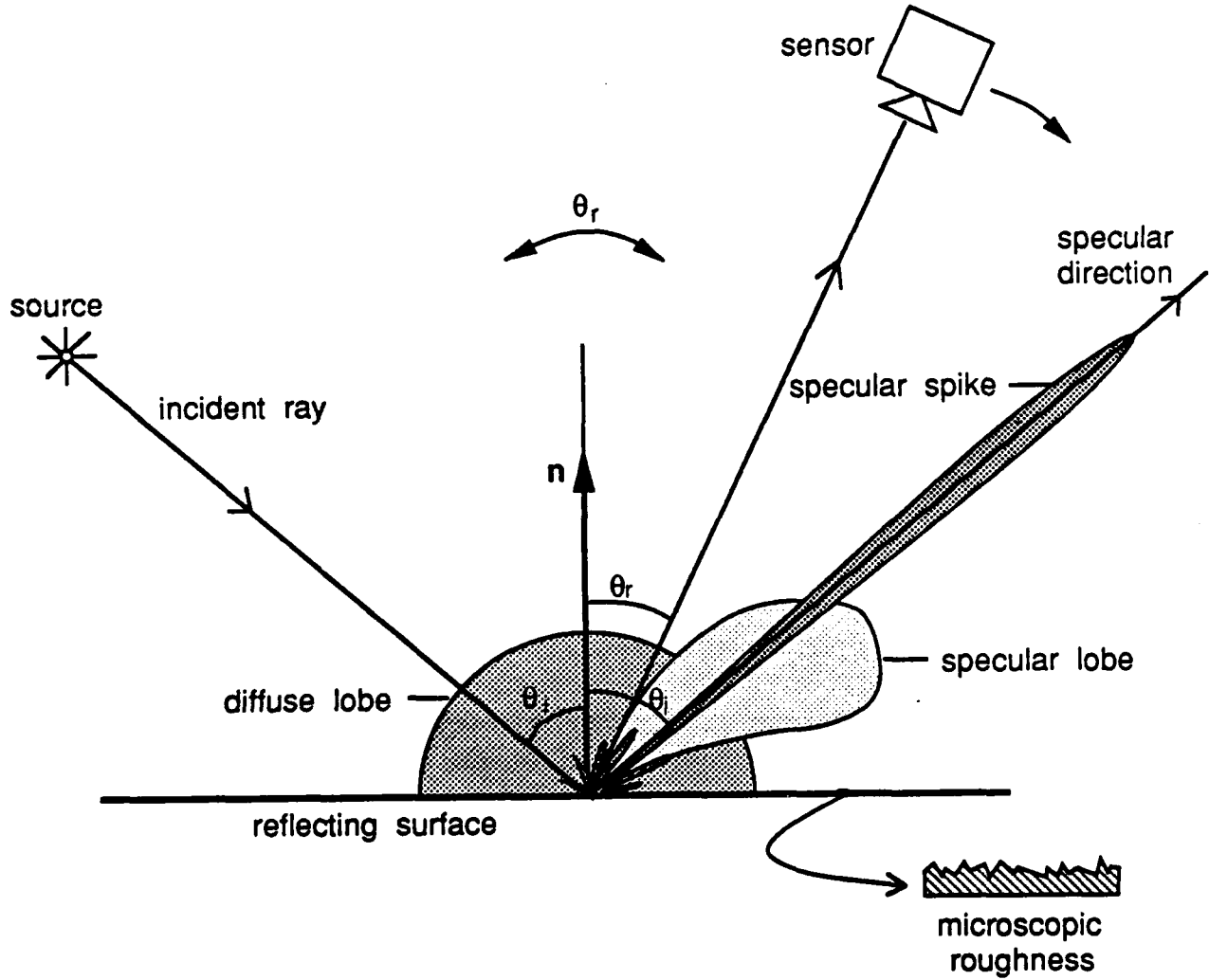


Figure 9: Polar plots of the three reflection components as functions of the viewing angle for a fixed source direction.

Given a geometry like in figure Figure 9 where the source light has a fixed direction and the sensor can be in any direction, an equation for the image irradiance I_{im} can be derived. This equation is a linear combination of the three reflection components:

$$I_{im} = C_{dl} + \frac{C_{sl}}{\cos\theta_r} \exp\left(-\frac{\alpha^2}{2\sigma_\alpha^2}\right) + C_{ss} \delta(\theta_i - \theta_r) \delta(\phi_r) \quad (9)$$

where, the constants C_{dl} , C_{sl} , and C_{ss} represent the strengths of the diffuse lobe, specular lobe, and specular spike components, respectively, θ_i and θ_r are the angles that form with the

surface normal vector the incident ray and the sensor direction respectively, ϕ_r is an angle which measures scattering directions that lie outside the *plane of incidence*. The specular spike component has been approximated as a double-delta function, meanwhile the specular lobe is represented by a one-dimensional normal distribution with mean value α and standard deviation σ_α .

3.3.2 Organization of the Simulator

The simulation process starts by reading a data file [7] which represents the scene to be simulated. The two main blocks of data in this file are the header and the body. The number of desired source lights, specifying their positions and directions towards they point to in a world coordinate frame, and source intensities are specified in the header of the file. The specific sensor being used is also defined in the header including its location (position and orientation) in the world frame, sensor resolution and aperture angle. Finally, the header must contain the background color selected for the scene.

The body of the data file describes the scene geometry using a boundary representation modeler. Every object is decomposed into its bounding surfaces. The location in the world frame and several physical parameters are required for every surface. These parameters correspond to surface features including color, texture, the reflectance parameters to be used in the reflectance model. The surface geometry is defined as a collection of triangular facets, each defined by three clockwise ordered vertices.

Once the input data has been read, the simulation begins. The ray-tracer process is shown in Figure 10. There are as many rays to be evaluated as the number of sensor pixels, which depends on the resolution of the sensor. The sensor is scanned row by row and a ray is computed at every column pixel using the sensor geometry and sensor parameters. The intersection point, the surface normal at this point and the surface reflectance parameters at such a point are extracted from the geometrical information of the scene whenever the actual ray intersects with any object in the scene. The reflectance model is then applied to all source lights. The incident direction is taken as the vector from the position of the corresponding source light to the intersection point. The reflected direction is based on the ray being evaluated. In this case the model gives the irradiance in the pixel area corresponding to the direct exposure of the surface to the light sources. The simulator also takes into account that the ray could result from multiple reflections or refraction of other rays. To do this, the process is recursively invoked to find if the possible reflected and refracted rays intersect with any surface of the scene. If so, the reflectance model is applied again. The tessellation performed in the previous stages constitutes valid geometric input data for the simulation process because the same boundary representation format is used in both cases.

Execution time of the simulation stage is also affected by the resolution of the used range images. Due to the fact that the geometric model is described with less boundary surfaces when resolution is reduced, it is easier to detect a possible ray intersection with the object.

3.3.3 Simulation Results

We have generated a sequence of 16 images by positioning both the sensor and one source light together in 16 different locations inside a plane which is parallel to the Y-Z plane and crosses

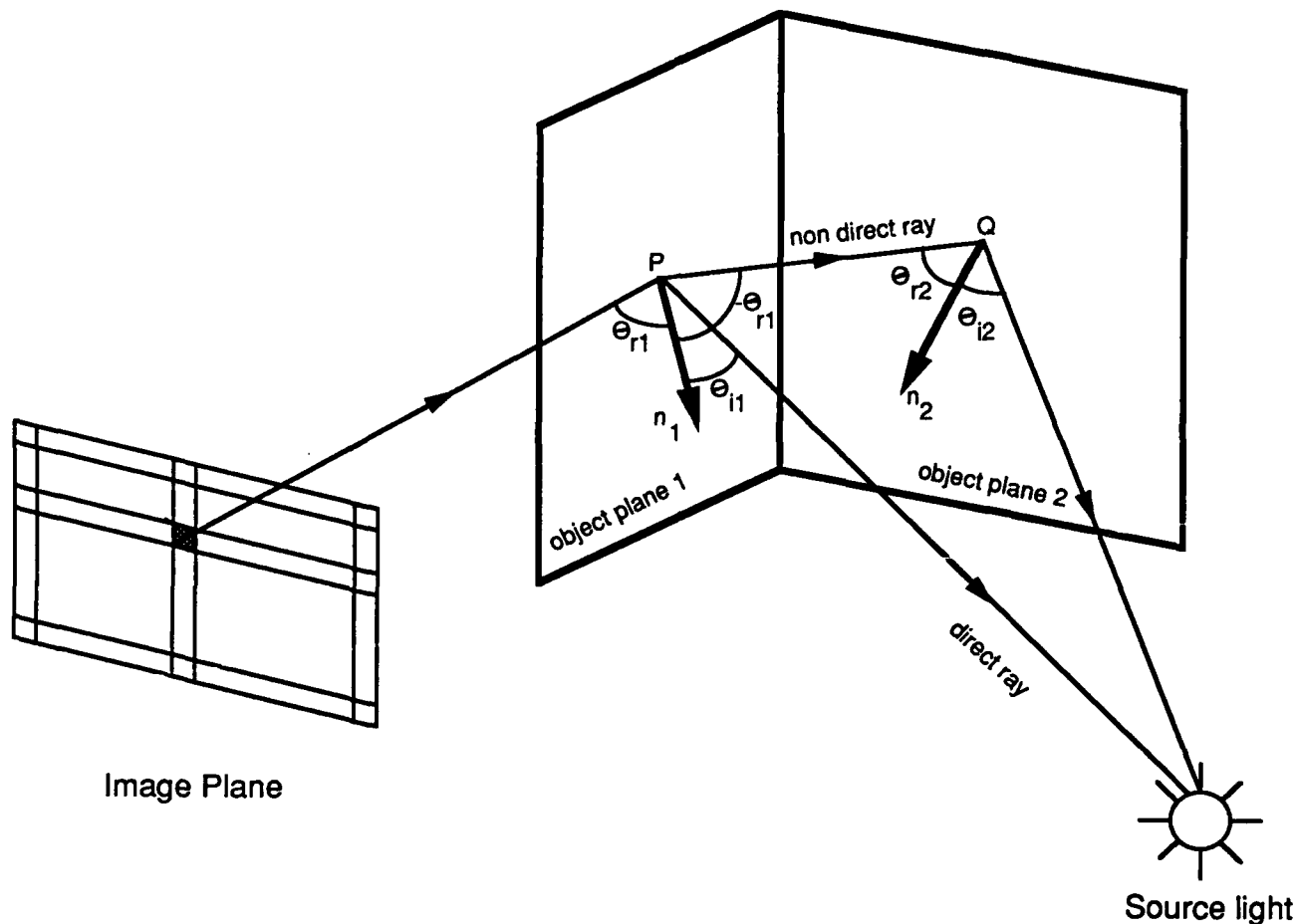


Figure 10: Geometry of the ray-tracer mechanism

the middle of the frame of the sculpture. The locations are equidistant from the center of the frame and separated from each other by a constant angular displacement of 10 degrees, being centered with respect to the front view (see Figure 11). Animation can be obtained on a monitor by sequentially displaying the 16 images.

Figure 12 shows several trials with three different materials: gold, steel and alabaster. They differ only in the color and the reflectance parameters associated to the surfaces, and for that reason they present different brightness levels between each other in the black and white reproduction of the Figure 11. In the lower right corner of the same Figure 11 another type of simulation is shown. In this case, the intensity value associate to each facet is not obtained from the reflectance model. It is computed by averaging three intensity values, coming from the original intensity image $I(i, j)$, corresponding to the three associated pixels of the triangular facet. In a sense, an intensity value which is related with the reflectance of the skin of the original face is "pasted" on top of every small patch of the face. For that reason the simulated image in this case

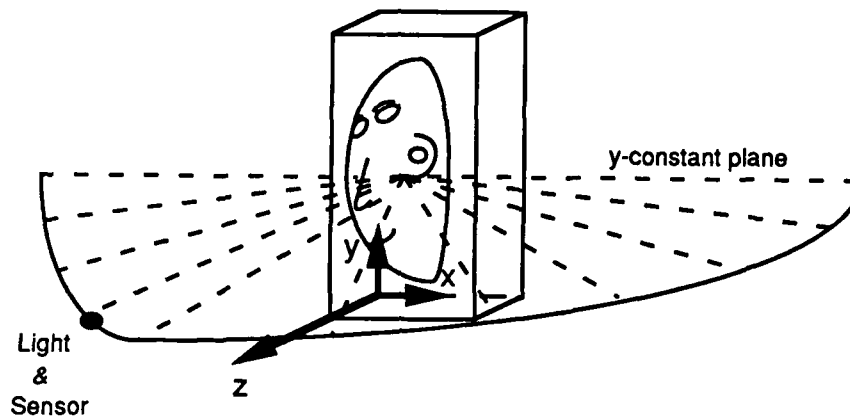


Figure 11: Sensor and source light geometric distribution to obtain 16 sequential images

resembles the human face in a more realistic fashion.

4 Rapid Fabrication Module

The capability to manufacture a wide variety of quality products in a timely and cost-effective response to market demands is the goal of today's manufacturing industry. The introduction of solid free form fabrication techniques is helping to achieve this goal and the improvement of global competitiveness. This new technology has the ability to rapidly produce prototypes and even the final parts directly from design models. Solid freeform fabrication processes are a relatively new class of fabrication technologies which build three-dimensional shapes by incremental material buildup of thin layers, and can make geometrically complex parts with little difficulty. These processes include selective laser sintering [4], laminated object manufacturing [3], ballistic powder metallurgy [9], three-dimensional printing [15] and stereolithography [5]. These processes are suited for rapidly producing physical prototypes from CAD representations.

This technology has never been applied to the generation of human faces, as used in this work. A rapid tool manufacturing system based on the integration of stereolithography and thermal spraying is described in [18]. They built a unified CAD/CAM tool manufacturing system testbed for an injection mold tooling paradigm. In this system, both prototyping and tooling fabrication are based upon compatible shaping deposition techniques. Choi [2] has reported an implementation where scanned data is automatically converted to surface and solid representation using a non-manifold geometric modeling system, NOODLES. After defining valid solid models, prototypes are fabricated with stereolithography, but no other further part fabrication is reported.

In the present work two processes based on shaping deposition techniques have also been used to deal with the physical reconstruction of the sculpture in steel: stereolithography and thermal spraying. The steel deposition process to create a 3-dimensional die shape is novel to this system. In the next sections the implementation details of the fabrication processes are described.

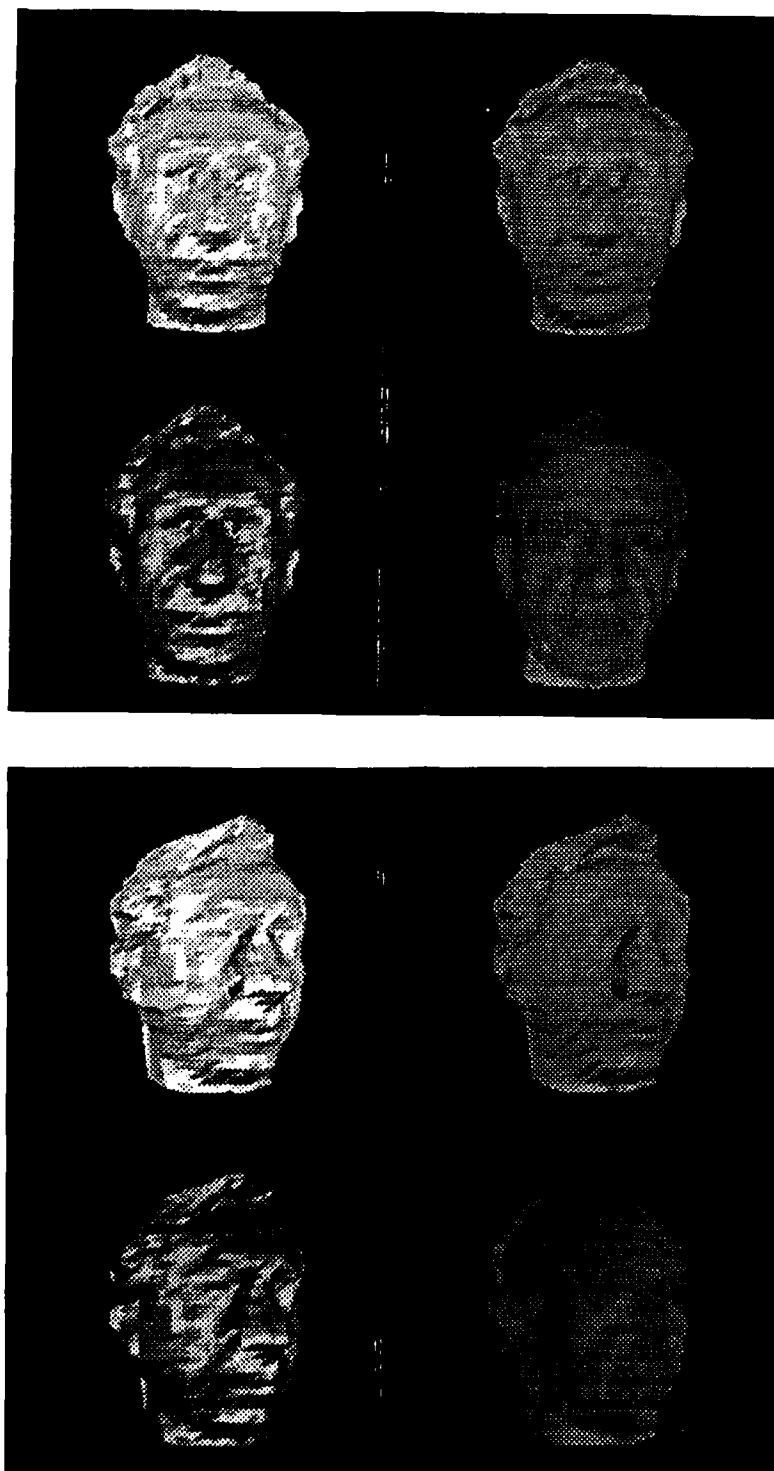


Figure 12: Images obtained considering different simulation conditions, relative to type of material and view direction

4.1 Stereolithography Process

Stereolithography is a technique which quickly builds plastic prototype parts, of arbitrary geometric complexity, based directly upon computer part models. The system described in this paper uses the commercially available stereolithography apparatus (SLA), Model 250, manufactured by 3D Systems, Inc. of Valencia, CA. The input to SLA is a linearized "tessellated" surface boundary representation of the part, and consists of a series of three sided facets and a corresponding facet normal. The Data Reconstruction Module transforms its internal representation to the tessellated format.

The SLA (Figure 13) is composed of a vat of photosensitive liquid polymer, an x-y scanning ultraviolet laser beam with a 0.25 mm (0.01 in.) beam diameter, and a z-axis elevator in the vat. The laser light is focused on the liquid's surface and cures the polymer, making solid forms wherever the liquid has scanned. The depth of cure is dosage-dependent. The physical object to be created, as described by the boundary representation model, is first "sliced" into the cross-sectional layers along the z-axis. For each slice, the laser's trajectory is dictated by the cross sections boundary and the bounded region.

The elevator platform is initially positioned at the surface of the liquid. As the laser draws a cross section in the x-y plane, a solid layer is formed on the elevator platform. The platform is lowered and then the next layer is drawn in the same way and adheres to the previous layer. The layers are typically between 0.13 and 0.5 mm (0.005 and 0.020 in.) thick. A three-dimensional plastic object thus grows in the vat, starting at the object's bottom and building to the top.

The current accuracy of SLA parts is of the order of 0.25 mm (0.010 in.) while surface texture is dependent on the building orientation. Additional postprocessing, such as carefully sanding and grinding the part, is therefore required for making accurate and smooth models. Since stereolithography is so new, rapid improvements are expected as the equipment and resins evolve with broadening commercial competition.

Figure 14 shows a picture of the plastic sculpture created with the SLA. Its actual dimensions are 4.8" long, 3.8" wide and 2.8" height. In this experience, the construction time was in the order of 48 hours. Build time is directly related with the volume of the photosensitive polymer to cure. In this sense, there was an unsuccessful previous experiment to build a different plastic prototype enclosed in a 10" by 10" frame instead of a 6" by 6" one. Stereolithography process crashed several times in this attempt due to power supply failures experienced after four or five days of running but before the final prototype ended. Simple computations demonstrate that this other prototype would require around eight days to be finished. A minor dependency on events like power supply failures could be achieved if the volume enclosed by the part is reduced. In this sense, a drastical improvement can be easily reachable by creating for example a hollow model of the face instead of the solid one.

4.2 Thermal Spraying Process

There are several thermal spraying processes available for depositing molten metal, ceramic, or plastic material. Our system uses electric arc spraying. In arc spraying (Figure 15), metal wire is

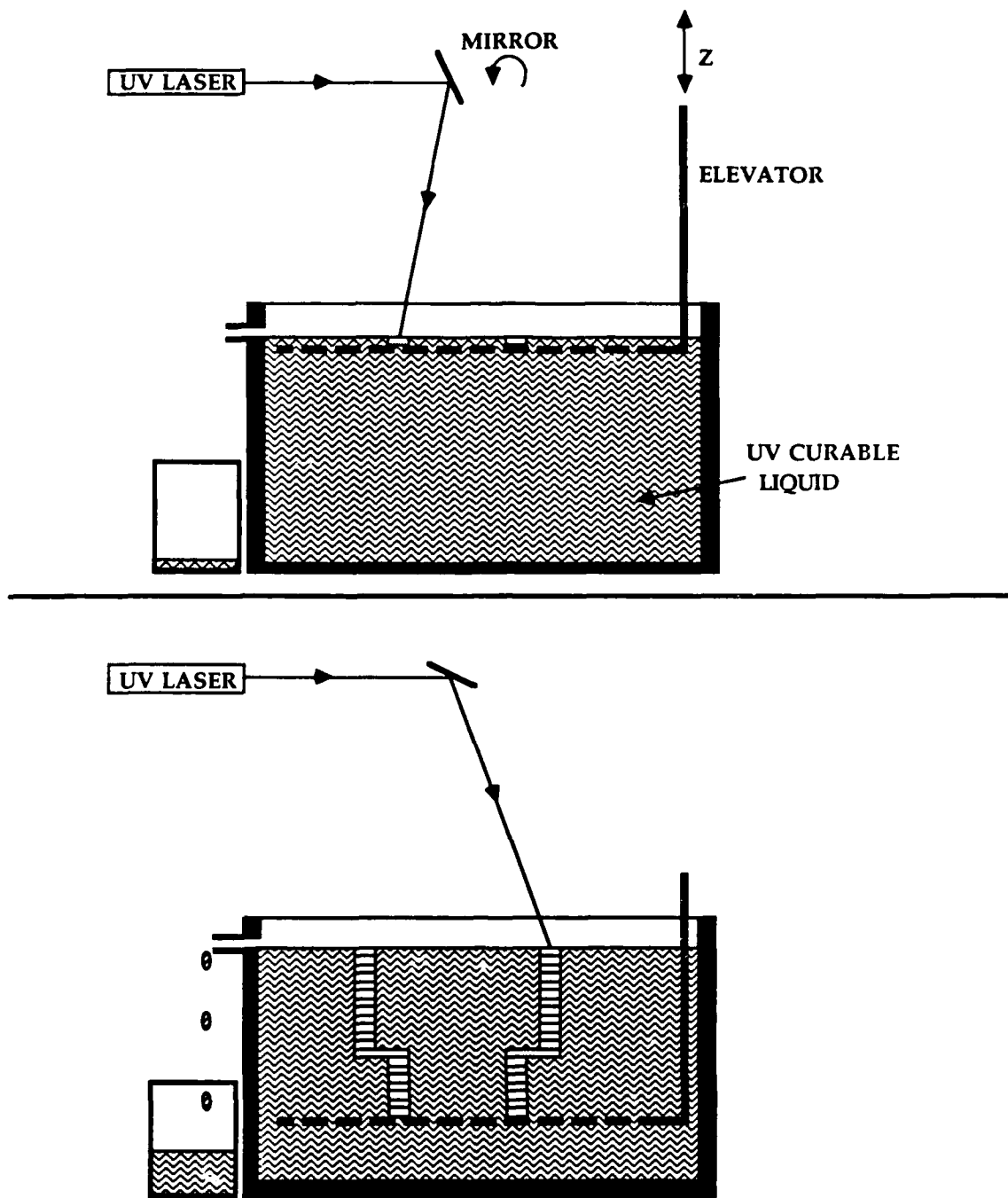


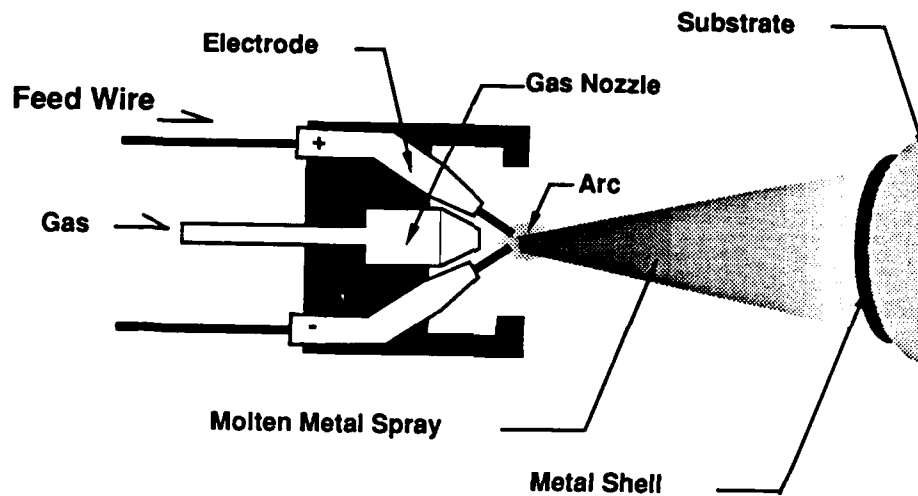
Figure 13: Stereolithography apparatus scheme



Figure 14: Aspect of the plastic sculpture

melted in an electric arc, atomized, and sprayed onto a substrate surface. On contact, the sprayed material rapidly solidifies and forms a surface coating. Spray coatings are built up by depositing multiple fused layers which, when separated from the substrate, form a free-standing shell with the shape of the substrate surface. By mounting the shell in a frame and backing it up with appropriate materials, a broad range of tools and dies can be fabricated including injection molds, forming dies, and EDM electrodes. For example, the cavities of injection molds can be fabricated by direct deposition of metal onto plastic SLA models of the desired part and backing the framed shell with epoxy resins or ceramic composites. Relative to conventional machining methods, the sprayed metal tooling approach has the potential to more quickly and less expensively produce tools, particularly for those parts with complex shapes (in particular free-flowing contours) or with large dimensions. Thus, with stereolithography, an initial part shape or prototype is quickly created. Thermal spraying is then used to make tools based on the part shapes produced by stereolithography.

Based on this concept the sprayed sculpture (i.e., equivalently a die) has been built using this process. An additional pattern transfer step is required for depositing steel. The fabrication steps are as follows (see Figure 16):



ARC SPRAY GUN

Figure 15: Electric arc spraying

- STEP 1: Built stereolithography pattern of face.
- STEP 2: Apply a release agent such as poly-vinyl alcohol or teflon to SLA pattern, and cast Cerro-metal onto pattern. The best replication is achieved by spraying Cerro-metal onto the pattern.
- STEP 3: Separate the SLA pattern from the newly created Cerro-metal pattern.
- STEP 4: Arc spray steel onto Cerro-metal pattern. The steel must be applied in thin layers and allowed to sufficiently cool between layers so as not to overheat the Cerro-metal. Sprayed steel bonds locally to the pattern by superficially melting and abrading a very thin layer of the low melt alloy. This creates an "anchor pattern" to increase coating adhesion. The alloy pattern thus shapes the sprayed steel and clamps it to the pattern surface. The clamping action is critical since sprayed steel has a tendency to warp and peel away from the pattern surface, and the clamping action counters this tendency. The steel is applied to a thickness of approximately 1.5 mm.
- STEP 5: Cast in a backing material to support the steel shell. Typical backing materials include epoxy mixed with aluminum or steel shot and ceramic composites.
- STEP 6: Melt away the Cerro-metal pattern by placing the pattern/shell/backing system into a furnace or by using a torch.

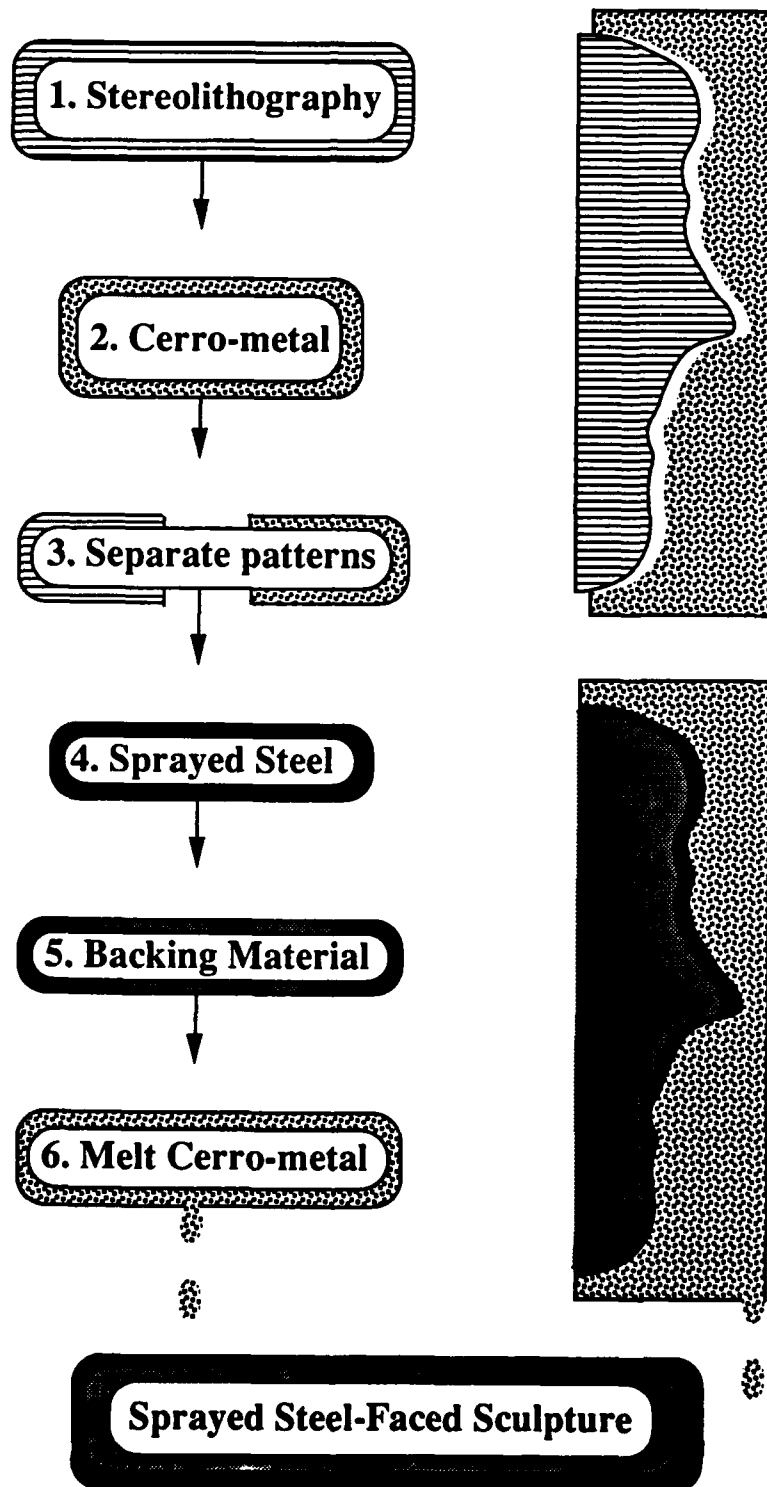


Figure 16: Graphical description of thermal spraying process

The result is the sprayed steel positive image of the sculpture which aspect appears in Figure 17.



Figure 17: Final aspect of the sculpture in steel

5 Summary

A 3D-object reconstruction system which integrates range image processing and rapid manufacturing techniques has been described in this paper. The goal of the system was to scan a human face and to reconstruct it in the form of a steel sculpture. An initial range image of the face is taken using a light-stripe range finder sensor. The range image is transformed into a solid model representation with the aid of image processing algorithms. The solid model is in the form of a tessellated surface boundary representation. A simulation process closes a feedback loop designed to check and refine data quality. Errors can be detected and corrected before proceeding with the fabrication process. Once the solid model has been refined, a plastic prototype of the sculpture is fabricated using stereolithography. The prototype is used as a negative mold pattern for a thermal

deposition process to build the final sculpture in the chosen material. Results for a 4.8" by 3.8" by 2.8" steel sculpture contained in a 6" by 6" frame has been presented along the paper.

Acknowledgements

The members of the VASC center at Carnegie Mellon University provided many useful suggestions. The authors are specially grateful to Yoshimasa Fujiwara for his participation in the simulation stage and Ye Mei who helped in the software development. Kevin Hartmann and Larry Schultz made possible the construction of both plastic prototype and steel sculpture.

References

- [1] P. Beckmann and A. Spizzichino, *The Scattering of Electromagnetic Waves from Rough Surfaces*, Pergamon Press, 1963.
- [2] Y. Choi, L. Weiss, E.L. Gursoz, and F.B. Prinz, *Rapid Prototyping from 3D Scanned Data through Automatic Surface and Solid Generation*, 1990 ASME Winter Annual Meeting.
- [3] D.P. Colley, *Instant Prototypes*, Mechanical Engineering, July 1988.
- [4] C.R. Deckard, *Recent Advance in Selective Laser Sintering*, Fourteenth Conference on Production Research and Technology, NSF, Ann Arbor, MI, October 1987.
- [5] D. Deitz, *Stereolithography Automates Prototyping*, Mechanical Engineering, 112(2), February 1990.
- [6] P. Finnigan, A. Hathaway, W. Loesen, *Merging CAT and FEM*, Mechanical Engineering, July 1990.
- [7] Y. Fujiwara, S. Nayar, K. Ikeuchi, *Appearance Simulator for Computer Vision Research* Technical Report, Carnegie Mellon University, Robotics Institute, Nov. 1990.
- [8] P.J. Garner, *New Mold Making Technique*, SPE Journal, 27 (5), May 1971.
- [9] D. Haubert, *Automated Fabrication of Net Shape Microcrystalline and Composite Metal Structures without Molds*, Manufacturing Processes, Systems and Machines: 14th Conference on Production Research and Technology, S.K. Samanta, Ed., NSF, Ann Arbor, MI, October 1987.
- [10] B. K. P. Horn and R. W. Sjoberg, *Calculating the reflectance map*, Applied Optics, Vol. 18, No. 11, pp. 1770-1779, June 1979.
- [11] B. K. P. Horn, *Robot Vision*, MIT Press, 1986.
- [12] A. F. Houchens and R. G. Hering, *Bidirectional Reflectance of Rough Metal Surfaces*, Thermophysics of Spacecraft and Planetary Bodies, G. B. Heller, Eds. Academic Press, 1967.
- [13] J. H. Lambert, *Photometria sive de mensura de gratibus luminis, colorum et umbrae*, Eberhard Klett, Augsburg, 1760.

- [14] S.K. Nayar, K. Ikeuchi and T. Kanade, *Surface reflection: Physical and geometrical perspectives*, Technical Report, CMU-RI-TR-89-7, Carnegie Mellon University, Robotics Institute, March 1989.
- [15] E. Sachs, *Three Dimensional Printing: Rapid Tooling and Prototypes directly from a CAD Model*, Advances in Manufacturing Systems Engineering, ASME, Winter Annual Meeting, 1989.
- [16] K.Sato, H. Yamamoto, and S. Inokuchi, *Range imaging system utilizing nematic liquid crystal mask*, International Conference on Computer Vision, pp.657-661, London, 1987.
- [17] K. Torrance and E. Sparrow, *Theory for Off-Specular Reflection from Roughened Surfaces*, Journal of the Optical Society of America, No. 57, pp. 1105-1114, 1967.
- [18] L.E. Weiss, E.L. Gursoz, F.B. Prinz, P.S Fussell, S. Mahalingham and E.P. Patrick, *A Rapid Tool Manufacturing System Based on Stereolithography and Thermal Spraying*, Manufacturing Review, vol 3, No.1, pp.40-48, March 1990.

APPENDIX A

A Reflectance Model Fundamentals

This appendix contains the basic formulation of the Beckmann-Spizzichino and Lambertian reflectance models, on top of which the simulation process used in this project has been built. More details about their integration in an unified reflectance model can be found in [14]

A.1 Beckmann-Spizzichino Model

The Beckmann and Spizzichino model uses physical optics to describe the reflection of plane waves from smooth and rough surfaces. Owing to the electromagnetic character of light, this model is directly applicable to the reflection of light by surfaces. A detailed derivation of this model, can be found in [1]. The intention here is to highlight the main equations involved in the model used in the simulator, and briefly show the assumptions under what they are derived.

Figure 18 represents the basic geometry for the Beckmann-Spizzichino model. Consider a plane wave incident on a surface, as shown in Figure 18. All vectors and surface points are defined using the Cartesian coordinates x, y, z with origin O and unit vectors \mathbf{x}, \mathbf{y} , and \mathbf{z} . Roughness of the surface can be represented by height distribution at every point (x, y) of the surface. In this sense, height distribution is a measurement of the irregularities of the surface at every point. The manner in which light is reflected by the The height of the surface is determined by the function $h = h(x, y)$, and the mean level of the surface is the plane $z = 0$. The location of the surface point Q is described by its displacement vector \mathbf{r} :

$$\mathbf{r} = x\mathbf{x} + y\mathbf{y} + h(x, y)\mathbf{z}. \quad (10)$$

All quantities associated with the incident field will be denoted by the subscript 1 and all those associated with the scattered field by the subscript 2. We will represent the plane wave by its electric field intensity only, keeping in mind that the magnetic field intensity may be determined from the electric field. The incident field at the surface point Q may be written as

$$\mathbf{E}_1 = E_{o1} \mathbf{e}_1 e^{-ik_1 \cdot \mathbf{r}} e^{i\omega t}, \quad (11)$$

where E_{o1} represents the electric field amplitude, \mathbf{e}_1 is the direction of the electric field, \mathbf{k}_1 is the wave propagation vector, and ω is the radian frequency of field oscillation.

We are interested in the instantaneous scattering of the incident plane wave by the surface. Hence, we can drop the second exponential term in the above equation that represent the temporal variation of the incident field. The incident propagation vector \mathbf{k}_1 will be assumed to always lie in the x - z plane of the coordinate frame. The angle of incidence θ_i of the plane wave is the angle between the propagation vector \mathbf{k}_1 and the z axis of our coordinate frame. If we are interested in the field scattered by the surface in the direction \mathbf{k}_2 , the corresponding scattering angle θ_r is the

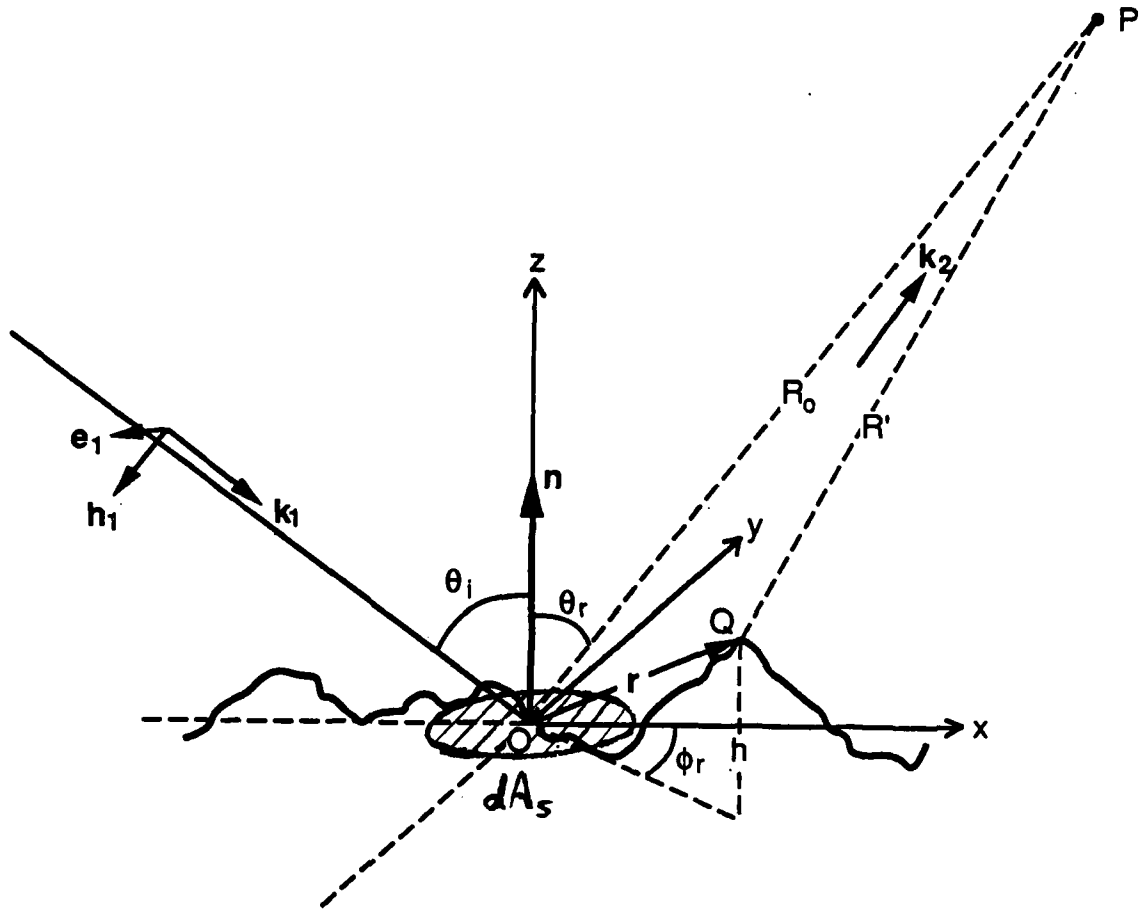


Figure 18: Coordinate system to derive the Beckmann-Spizzichino model

angle between k_2 and the z axis. For scattering directions that lie outside the *plane of incidence* (k_1, z), we must introduce an additional angle ϕ_r , as shown in Figure 18. The propagation constant k corresponding to the propagation vectors k_1 and k_2 is related to the wavelength λ of the incident wave by equation:

$$k = \frac{2\pi}{\lambda}. \quad (12)$$

From here on, we will assume the polarization of the incident wave to be either parallel or perpendicular, and the incident field will be denoted by the scalar E_I , where

$$E_I = e_1 E_1. \quad (13)$$

When incident plane wave strikes the surface, various physical phenomena occur, ending with the generation of a resultant field $(E)_s$ that at a given surface point Q must satisfy the *wave equation*:

$$\Delta^2(E)_S + k^2(E)_S = 0. \quad (14)$$

where k is once again the propagation constant. Therefore, the field $(E)_S$ at the surface may be determined by solving the wave equation for the boundary conditions imposed by the surface profile.

The field scattered by the surface in any direction can be determined from the field at the surface. Let P be the point of observation and let the variable R' denote the distance between P and points on the surface S , as shown in Figure 18. We would like to find the scattered field E_z at the point P . To this end, let us consider a volume V that is bounded almost everywhere by the surface S but is extended such that the point P lies just outside the volume. Therefore, it is reasonable to assume that the field $(E)_S$ is continuous and the above wave equation must be satisfied everywhere inside V . Further, the field at a point inside the volume that is nearest to P will experience almost the same field as the point P . Using these assumptions and Green's first and second theorems, the scattered field $E_z(P)$ at the point P can be determined [1] from equation 14 as:

$$E_z(P) = \frac{1}{4\pi} \iint \left((E)_S \frac{\partial \psi}{\partial n} - \psi \left(\frac{\partial E}{\partial n} \right)_S \right) dS, \quad (15)$$

where

$$\psi = \frac{e^{ikR'}}{R'}. \quad (16)$$

This is called the *Helmholtz integral* that provides us the solution of the wave equation at any point inside (P is almost inside) of a region in terms of the values of the function (surface field $(E)_S$) and its normal derivative on the boundary (surface S) of the region.

In order to evaluate the above integral, we must find $(E)_S$ and $(\partial E / \partial n)_S$, i.e. the field and its normal derivative on the surface S . In general, these two quantities are unknown. *Kirchoff's assumption* may be used to approximate the values of the field and its normal derivative at each point on the surface. The approximation is obtained by assuming that the surface is locally planar (the surface does not have any sharp edges) and thus the field at a point on the surface is equal to the field that would be present on a tangent plane at that point. Under this assumption, the field on S may be determined as

$$(E)_S = (1 + F) E_i \quad (17)$$

and by differentiating the above equation, the normal derivative of the field is determined as

$$\left(\frac{\partial E}{\partial n} \right)_S = (1 - F) E_i \mathbf{k}_i \cdot \mathbf{n}', \quad (18)$$

where \mathbf{n}' is the normal to the surface at the point under consideration and F is the *Fresnel reflection coefficient* for a smooth plane.

Let us assume now that the surface under consideration is a rectangular patch of area A and dimensions $2X$ and $2Y$ in the x and y directions, respectively, i.e. $A = 4XY$. Further, we assume that the observation point P is at a great distance from the surface compared to the physical dimensions of the surface patch. Therefore, it is seen from Figure 18 that, for any surface point, the distance R' can be expressed in terms of the distance R_o and the displacement vector \mathbf{r} as

$$k R' = k R_o - \mathbf{k}_2 \cdot \mathbf{r}. \quad (19)$$

By substituting equations 17, 18, and 19 in equation 15, we can express the scattered field E_2 as

$$E_2 = \frac{E_o i k e^{i k R_o}}{4 \pi R_o} \int_{-X}^X \int_{-Y}^Y (a h'_x + c h'_y - b) e^{i \mathbf{v} \cdot \mathbf{r}} dx dy, \quad (20)$$

where

$$\begin{aligned} \mathbf{v} &= (v_x, v_y, v_z) = k(\sin\theta_i - \sin\theta_r \cos\phi_r) \mathbf{x} + k \sin\theta_r \sin\phi_r \mathbf{y} - k(\cos\theta_i + \cos\theta_r) \mathbf{z} \\ a &= (1 - F) \sin\theta_i + (1 + F) \sin\theta_r \cos\phi_r \\ b &= (1 + F) \cos\theta_r - (1 - F) \cos\theta_i \\ c &= -(1 + F) \sin\theta_r \sin\phi_r \end{aligned} \quad (21)$$

and the terms h'_x and h'_y denote the slopes of the surface $h(x, y)$ in the x and y directions, respectively.

This integral is easier to evaluate under the assumption of considering the surface medium to be a perfect conductor. In this case the terms a , b and c in equation 20 are independent of x and y . We also assume the incident wave to be of perpendicular polarization, i.e. $F = -1$.

It can be seen that for a perfect smooth surface, where $h = 0$, $h'_x = 0$, and $h'_y = 0$, the scattered field is obtained with ease. However, a perfectly smooth surface is only the limiting case of a rough one. We will assume that our surface has random irregularities. By using a statistical model for the irregularities, we can predict the reflection characteristics of the surface. The uncertainty in height of a surface point can be described by a probability distribution function. Though Beckmann and Spizzichino have discussed a variety of distributions, they consider the normal distribution to be the most important and typical of a rough surface.

The normal height distribution uses the following parameters. The surface height has the mean value $\langle h \rangle = 0$, standard deviation σ_h , and correlation distance T . Since h and the scattered field E_2 are related by equation 20, the statistics of E_2 can be determined from the statistics of h . Beckmann and Spizzichino only use the mean field $\langle E_2 \rangle$ as a stepping stone to derive the mean

scattered power $\langle E_2 E_2^* \rangle = \langle |E_2|^2 \rangle$. For an angle on incidence θ_i , the mean power scattered in the direction (θ_r, ϕ_r) by a rough surface, whose height h is normally distributed with mean value $\langle h \rangle = 0$, standard deviation σ_h , and correlation distance T , is given by

$$\langle E_2 E_2^* \rangle = \frac{E_o^2 A^2 \cos^2 \theta_i}{\lambda^2 R_o^2} e^{-g} \left(\rho_o^2 + \frac{\pi T^2 D^2}{A} \sum_{m=1}^{m=\infty} \frac{g^m}{m! m} e^{-v_{xy}^2 T^2 / 4m} \right), \quad (22)$$

where

$$g = \left(2\pi \frac{\sigma_h}{\lambda} (\cos \theta_i + \cos \theta_r) \right)^2 \quad (23)$$

$$\rho_o = \text{sinc}(v_x X) \text{sinc}(v_y Y) \quad (24)$$

$$D = \left(\frac{1 + \cos \theta_i \cos \theta_r - \sin \theta_i \sin \theta_r \cos \phi_r}{\cos \theta_i (\cos \theta_i + \cos \theta_r)} \right) \quad (25)$$

$$v_{xy} = \sqrt{v_x^2 + v_y^2}. \quad (26)$$

We see from equation 23 that the factor g in equation 22 depends on λ . Raleigh criterion states that the roughness of a surface can be expressed as a function of λ . In this sense, g represents the roughness of the surface and the three cases $g \ll 1$, $g \approx 1$, and $g \gg 1$ correspond to smooth¹ surfaces, moderately rough surfaces, and rough surfaces, respectively. It is important to note that the model under consideration only attempts to describe the reflection mechanism that is often referred to by the vision research community as "specular reflection". As seen from equation 22, the mean scattered power is the sum of two terms. The first term $e^{-g} \rho_o^2$ is the "specular spike" component of the specular reflection and represents the only the field scattered very close to the specular direction. It is seen from equation 24, that when the surface dimensions are small, ρ_o becomes a very sharp function of θ_i and θ_r and is equal to zero for any direction of scattering except a narrow range about the specular direction. Since the mean slope of the surface is constant and is independent of the roughness of the surface, a privileged scattering in the specular direction is expected. The second term in equation 22 corresponds to the "specular lobe"², i.e. the diffusely scattered field that results from the roughness of the surface. The specular lobe component is distributed around the specular direction. For a perfectly smooth surface, $g = 0$ and the specular lobe vanishes while the specular spike is strong. As the roughness measure g increases, the spike component shrinks rapidly, while the lobe component increases in magnitude. The exponential series given by the summation in the lobe component may be approximated for smooth ($g \ll 1$) and very rough ($g \gg 1$) surfaces. The approximations result in simpler expressions for the scattered power for these two extreme surface conditions:

¹We define a smooth surface as one that is either perfectly smooth or "slightly" rough.

²Beckmann and Spizzichino have referred to this component as the "diffuse" component. The term "diffuse" has historically been used by the vision community to describe the reflection component that results from other mechanisms such as multiple reflections and internal scattering. To avoid confusion we will refer to the diffuse component of specular reflection as the specular lobe.

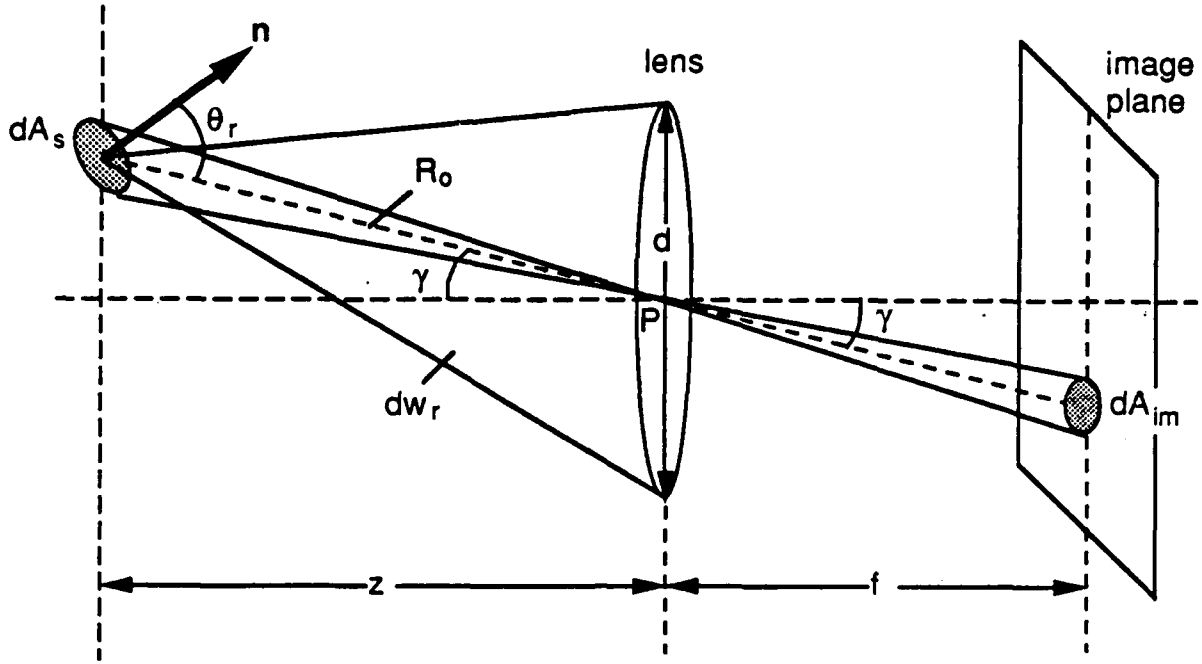


Figure 19: Image formation: light waves radiated by the surface area dA_s and gathered by the lens are projected onto an area dA_{im} on the image plane. Adapted from [11].

$$\langle E_z E_z^* \rangle_{smooth} = \frac{E_o^2 A^2 \cos^2 \theta_i}{\lambda^2 R_o^2} e^{-g} \left(\rho_o^2 + \frac{\pi T^2 D^2 g}{A} e^{-v_{xy}^2 T^2/4} \right) \quad (g \ll 1) \quad (27)$$

$$\langle E_z E_z^* \rangle_{rough} = \frac{E_o^2 A \cos^2 \theta_i \pi T^2 D^2}{\lambda^2 R_o^2 v_z^2 \sigma_h^2} \exp \left(\frac{-v_{xy}^2 T^2}{4 v_z^2 \sigma_h^2} \right) \quad (g \gg 1) \quad (28)$$

The above equations for scattered power represent the Beckmann-Spizzichino reflectance model. Anyway, we are interested in the radiance of the surface, L_r which is defined as the energy of light emitted per unit fore-shortened area per unit solid angle. Surface radiance can be related to image irradiance I_{im} which we are specially interested in, because we want to simulate an image taking from a given scene. Image irradiance I_{im} is defined as the incident flux density in a surface of the image plane.

Consider the image formation geometry shown in Figure 19. The surface radiance derived for this geometry ([10]) is given by the following expression:

$$L_r = \frac{1}{2} \sqrt{\frac{\mu}{\epsilon}} \frac{R_o^2 f^2 \langle E_z E_z^* \rangle}{z^2 dA_i \cos \gamma} \quad (29)$$

where ϵ and μ are the *permittivity* and *permeability* of the medium in which the wave is propagated, and dA_i represents the image element area (pixel) which is constant for a given sensor.

By substituting equation 22 in 29 we obtain:

$$L_r = \sqrt{\frac{\mu}{\epsilon}} \frac{E_o^2 \cos^2 \theta_i}{2 \lambda^2 \cos \gamma} e^{-g} \left(\left(\frac{z}{f} \right)^2 \frac{dA_i}{\cos^2 \theta_r} \rho_o^2 + \frac{\pi T^2 D^2}{\cos \theta_r} \sum_{m=1}^{\infty} \frac{g^m}{m! m} e^{-v_{xy}^2 T^2 / 4m} \right) \quad (30)$$

Similarly, from equations (27) and (28), the surface radiance for smooth and rough surfaces may be written as

$$L_{r, smooth} = \sqrt{\frac{\mu}{\epsilon}} \frac{E_o^2 \cos^2 \theta_i}{2 \lambda^2 \cos \gamma} e^{-g} \left(\left(\frac{z}{f} \right)^2 \frac{dA_i}{\cos^2 \theta_r} \rho_o^2 + \frac{\pi T^2 D^2 g}{\cos \theta_r} \right) \quad (g \ll 1) \quad (31)$$

$$L_{r, rough} = \sqrt{\frac{\mu}{\epsilon}} \frac{E_o^2 \cos^2 \theta_i \pi T^2 D^2}{2 \lambda^2 \cos \gamma \cos \theta_r v_z^2 \sigma_h^2} \exp \left(\frac{-v_{xy}^2 T^2}{4 v_z^2 \sigma_h^2} \right) \quad (g \gg 1) \quad (32)$$

Using the same imaging geometry shown in Figure 19, Horn [11] has established a relationship between surface radiance L_r and image irradiance I_{im} . The image irradiance is found to be proportional to surface radiance and can be expressed as

$$I_{im} = L_r \frac{\pi}{4} \left(\frac{d}{f} \right)^2 \cos^4 \gamma. \quad (33)$$

When the image covers only a narrow angle of the scene, we see that $\gamma \approx 0$ and it is reasonable to assume that $\cos \gamma = 1$ in the above equations.

A.2 Lambertian Model

When light strikes on a surface area dA , like in Figure 18, some of the light passes through the surface and the remaining portion is reflected. Light penetrating the surface area hits internal pigments of an object, is partly absorbed, and is randomly emitted. We will refer to this reflection component as the *Lambertian component*. The incident flux on the surface, $d^2 \Phi_i$ is given as $L_i d\omega_i dA \cos \theta_i$. The surface irradiance, I_s is determined by dividing the incident flux by the surface area, dA . Thus,

$$I_s = L_i d\omega_i \cos \theta_i. \quad (34)$$

Since $L_{r, lamb}$, the surface radiance given by the Lambertian component, is proportional to the irradiance of the surface given by a light source [13], and K_{lamb} is a proportional constant, we can state the following formula:

$$L_{r, lamb} = K_{lamb} L_i d\omega_i \cos \theta_i \quad (35)$$

This equation is known as Lambertian's cosine law. Image irradiance due to Lambertian component is also obtained from equation 33